

# 2001-2022 global gross primary productivity dataset using an ensemble model based on random forest

Xin Chen<sup>1</sup>, Tiexi Chen<sup>1,2,3\*</sup>, Xiaodong Li<sup>4</sup>, Yuanfang Chai<sup>5</sup>, Shengjie Zhou<sup>1</sup>, Renjie Guo<sup>6</sup>, Jie Dai<sup>1</sup>

<sup>1</sup>School of Geographical Sciences, Nanjing University of Information Science and Technology, Nanjing 210044, Jiangsu, China.

<sup>2</sup>Qinghai Provincial Key Laboratory of Plateau Climate Change and Corresponding Ecological and Environmental Effects, Qinghai University of Science and Technology, Xining 810016, China

<sup>3</sup>School of Geographical Sciences, Qinghai Normal University, Xining 810008, Qinghai, China.

<sup>4</sup>Qinghai Institute of Meteorological Science, Xining 810008, Qinghai, China.

<sup>5</sup>Department of Earth Sciences, Vrije Universiteit Amsterdam, Boelelaan 1085, 1081 HV, Amsterdam, the Netherlands

<sup>6</sup>Faculty of Geographical Science, Beijing Normal University, Beijing, China.

Correspondence to: Tiexi Chen (txchen@nuist.edu.cn)

**Abstract.** Advancements in remote sensing technology have significantly contributed to the improvement of models for estimating terrestrial gross primary productivity (GPP). However, discrepancies in the spatial distribution and interannual variability within GPP datasets pose challenges to a comprehensive understanding of the terrestrial carbon cycle. In contrast to previous models that rely on remote sensing and environmental variables, we developed an ensemble model based on the random forest (ERF model). This model used ~~the~~ GPP outputs from established models (EC-LUE, GPP-kNDVI, GPP-NIRv, Revised-EC-LUE, VPM, MODIS) as inputs to estimate GPP. The ERF model demonstrated superior performance, explaining 85.1% of the monthly GPP variations at 170 sites ~~and~~, surpassing the performance of ~~both~~ selected GPP models (67.7%-77.5%) and an independent random forest model using remote sensing and environmental variables (81.5%). Additionally, the ERF model ~~improved~~ the accuracy across each month and various subvalues, mitigating the issue of "high value underestimation and low value overestimation" in GPP estimates. Over the period from 2001 to 2022, the global GPP estimated by the ERF model was 132.7 PgC yr<sup>-1</sup>, with an increasing trend of 0.42 PgC yr<sup>-2</sup>, which is comparable to or slightly better than the accuracy of other mainstream GPP datasets in term of validation results of GPP observations independent of FLUXNET (ChinaFlux) from ChinaFlux. Importantly, for the growing number of GPP datasets, our study provides a way to integrate these GPP datasets, which may lead to a more reliable estimate of global GPP. In summary, the ERF model offers a reliable alternative for reducing uncertainties in GPP estimate, providing a more dependable global GPP estimate.

## 32 1 Introduction

33 Gross primary productivity (GPP) is the largest carbon flux in the global carbon cycle, and serves as the primary input of  
34 carbon into the terrestrial carbon cycle. Uncertainties in GPP estimates can propagate to other carbon flux estimates, making  
35 it crucial to clarify the spatio-temporal patterns of GPP (Xiao et al., 2019; Ruehr et al., 2023). However, global GPP is variously  
36 estimated from 90 PgC yr<sup>-1</sup> to 160 PgC yr<sup>-1</sup> across different studies, with these variations becoming more pronounced when  
37 scaled down to regional scales or specific ecosystem types. This variability underscores the necessity for innovative methods  
38 to reduce the uncertainty in GPP estimates (Jung et al., 2019; Ryu et al., 2019; Anav et al., 2015).

39 The light use efficiency (LUE) model is one of the most widely adopted methods for estimating GPP. It assumes that GPP is  
40 proportional to the photosynthetically active radiation absorbed by vegetation, and optimizes the spatio-temporal pattern of  
41 GPP through meteorological constraints such as temperature and moisture (Pei et al., 2022). However, variations in these  
42 constraints varies significantly, leading to differences of over 10% in model explanatory power. (Yuan et al., 2014). Recent  
43 studies have proposed some novel vegetation indices that have been shown to be effective proxies for GPP through theoretical  
44 derivation and observed validation (Badgley et al., 2017; Camps-Valls et al., 2021). However, these vegetation indices often  
45 use only remote sensing data as an input for estimating long-term GPP without considering meteorological factors, which has  
46 led to some controversy (Chen et al., 2024; Dechant et al., 2020; Dechant et al., 2022). Both LUE and vegetation index models  
47 use a combination of linear mathematical formulas to estimate GPP. However, but ecosystems are inherently complex, and  
48 the biases introduced by these numerical models increase the uncertainty in the GPP estimates of the final product (GPP).  
49 Machine learning models have shown great potential for improving GPP estimates in previous studies (Jung et al., 2020; Guo  
50 et al., 2023). These model are trained by non-physical means directly using GPP observations and selected environmental and  
51 vegetation variables, and the performance of the models depends on the number and quality of observed data and the  
52 representativeness of input data. Nevertheless, direct validation from flux towers of FLUXNET reveals that these models  
53 typically explain only about 70% of monthly GPP variations, with similar performance to other GPP models (Wang et al.,  
54 2021; Badgley et al., 2019; Zheng et al., 2020; Jung et al., 2020). Due to deviations in the model structure, a common limitation  
55 across these models is the poor estimate of monthly extreme GPP, leading to the phenomenon of "high value overestimation  
56 and low value overestimation" (Zheng et al., 2020). Especially for extremely high values, which usually occur during the  
57 growing season and largely determine the annual total value and interannual fluctuations of GPP, this underestimation may  
58 hinder our understanding of the global carbon cycle.

59 It is challenging for a single model to provide accurate estimates for all global regions. Ensemble models have  
60 outperformed have been shown to outperform individual single models in previous studies, potentially addressing some inherent  
61 issues in model estimate (Chen et al., 2020; Yao et al., 2014). Traditional multi-model ensemble methods usually use a simple  
62 multi-model average or a weighted Bayesian average. However, these methods typically assign fixed weights to each model  
63 and are essentially linear combinations. Recent studies have incorporated applied machine learning techniques methods to  
64 multi-model ensembles to establish nonlinear relationships between multiple simulated target variables and real target variable,

65 improving simulation performance (Bai et al., 2021; Yao et al., 2017; Tian et al., 2023). Whether this method can improve  
66 some common problems with ~~individual GPP models~~~~a single GPP model~~, such as high value underestimation and low value  
67 overestimation, is not clear and needs to further investigation.  
68 In this study, we attempt to use an ensemble model based on the random forest (ERF model) to improve global GPP estimate.  
69 Specifically, the work of this study includes the following: (1) Recalibrating ~~the~~ parameters for each model, and comparing  
70 the performance of six GPP models and the ERF model; (2) Focusing on the phenomenon of “high value underestimation and  
71 low value overestimation” in each model, and evaluating the performance of each model ~~across~~ different months, vegetation  
72 types and subvalues (high value, median value, low value); (3) Developing a global GPP dataset using the ERF model and  
73 ~~validating~~~~validate~~ its generalization using GPP observations from ChinaFlux.

## 74 2 Method

### 75 2.1 Data at the global scale

76 In this study, we selected remote sensing data from the Moderate Resolution Imaging Spectroradiometer (MODIS) and  
77 meteorological data from ERA5 to estimate global GPP (Hersbach et al., 2020). For the remote sensing data, surface reflectance  
78 (red band, near infrared band, blue band and shortwave infrared band), leaf area index (LAI) and fraction of photosynthetically  
79 active radiation (FPAR) were used. For meteorological data, we selected average air temperature, dew point temperature,  
80 minimum air temperature, total solar radiation and direct solar radiation. Dew point temperature and air temperature were used  
81 to calculate saturated vapor pressure difference (VPD) (Yuan et al., 2019), and diffuse solar radiation (DifSR) was derived as  
82 the difference between total solar radiation and direct solar radiation. Minimum air temperature was obtained from the hourly  
83 air temperature. CO<sub>2</sub> data were obtained from the monthly average carbon dioxide levels measured by the Mauna Loa  
84 Observatory in Hawaii. Table 1 provides an overview of the datasets used in this study.

85

86 **Table 1.** Overview of the datasets used in this study.

Variable	Dataset	Spatial resolution	Temporal resolution	Temporal coverage
Surface reflectance (red band and near infrared band)	MCD43C4	0.05 °	daily	2001-2022
Surface reflectance (red band, near infrared band, blue band and shortwave infrared band)	MOD09CMG	0.05 °	daily	2001-2022
LAI	MOD15A2H	500m	8d	2001-2022
FPAR	MOD15A2H	500m	8d	2001-2022
Average air temperature (AT)	ERA5-land	0.1 °	Monthly	2001-2022

Dew point temperature (DPT)	ERA5-land	0.1 °	Monthly	2001-2022
Minimum air temperature (MINT)	ERA5-land	0.1 °	Monthly	2001-2022
Total solar radiation (TSR)	ERA5 monthly data on single levels	0.25 °	Monthly	2001-2022
Direct solar radiation (DirSR)	ERA5 monthly data on single levels	0.25 °	Monthly	2001-2022
CO <sub>2</sub>	NOAA's Earth System Research Laboratory	/	Monthly	2001-2022
Distribution map of C4 crops	Harvested Area and Yield for 175 Crops	1/12 °	Annual	2000
Land use	MCD12C1	0.05 °	Annual	2010

87

88 Previous studies have shown that the photosynthetic capacity of C4 crops is much higher than that of C3 crops (Chen et al.,  
89 2014; Chen et al., 2011), so it is necessary to divide the cropland into C3 crops and C4 crops. To estimate the global GPP, we  
90 used the ~~dataset~~ "175 Crop harvested Area and yield" dataset, which describes the global harvested area and yield of 175 crops  
91 in 2000 (Monfreda et al., 2008). We extracted the sum of the area ratios of all C4 crops (corn, corn feed, sorghum, sorghum  
92 feed, sugarcane, millet) at each grid as the coverage of C4 crops (Figure S1). Consequently, the estimated value of cropland  
93 GPP can be expressed as: coverage of C3 crops × simulated GPP value of C3 crops + coverage of C4 crops × simulated GPP  
94 value of C4 crops, which ~~has been used~~ ~~was used~~ in a previous study (Guo et al., 2023).

95 The land use map was derived from the IGBP classification of MCD12QC1, and 2010 was chosen as the reference year (that  
96 is, land use data is unchanged in the simulation of global GPP). In order to meet the requirements of subsequent research, land  
97 cover types were grouped into 9 categories: Deciduous Broadleaf Forest (DBF), Evergreen Needleleaved Forest (ENF),  
98 Evergreen Broadleaf Forest (EBF), Mixed Forest (MF), Grassland (GRA), Cropland (including CRO-C3 and CRO-C4),  
99 Savannah (SAV), Shrub (SHR), Wetland (WET).

100 Finally, for higher resolution data, we gridded the dataset to 0.05 ° by averaging all pixels whose center fell within each 0.05 °  
101 grid cell for upscaling. For lower resolution data, we used the nearest neighbor resampling method to 0.05 °. In addition,  
102 MODIS data were aggregated to a monthly scale to ensure spatio-temporal consistency.

## 103 2.2 Observation data at the site scale

104 GPP observations were sourced from the FLUXNET 2015 dataset, which includes carbon fluxes and meteorological variables  
105 from more than 200 flux sites around the world (Pastorello et al., 2020). GPP cannot be obtained directly from flux sites and  
106 usually needs to be obtained by dismantling the Net Ecosystem Exchange. We chose a monthly level GPP based on the  
107 nighttime partitioning method and retained only high quality data ( $NEE\_VUT\_REF\_QC > 0.8$ ) for every year, ultimately  
108 selecting 170 sites with 10932 monthly values for this study. In addition, we selected monthly average air temperature, total  
109 solar radiation and VPD. The site observations do not provide direct solar radiation, so we extracted data from ~~the~~ ERA5  
110 covering the flux tower. Monthly minimum air temperature was derived from hourly air temperature. Since some required  
111 model data are not directly available at flux sites, LAI and FPAR were extracted from MOD15A2H (500 m), and surface  
112 reflectance data (red band, near infrared band, blue band and shortwave infrared band) were derived from MCD43A4 (500 m)  
113 and MOD09A1 (500 m). These data are roughly similar to the footprint of the flux site and can represent the land surface of  
114 the site (Chu et al., 2021).

## 115 2.3 GPP estimation model

116 We selected six independent models to estimate GPP in this study. These models are widely used with few model parameters  
117 and have demonstrated reliable accuracy in previous studies (Zheng et al., 2020; Zhang et al., 2017; Badgley et al., 2017). The  
118 six models are EC-LUE, Revised-EC-LUE, NIRv-based linear model, kNDVI-based linear model, VPM, MODIS. The VPM,  
119 MODIS and EC-LUE are LUE models based on remote sensing data and meteorological data (Yuan et al., 2007; Running et  
120 al., 2004; Xiao et al., 2004). ~~Recently,~~ Zheng et al., (2020) proposed the Revised-EC-LUE model, which divides the canopy  
121 into sunlit and shaded leaves, improving the estimation of global GPP (Zheng et al., 2020). The NIRv and kNDVI are  
122 ~~newly novel proposed~~ vegetation indices calculated from the red and near-infrared bands of the reflectance spectrum (Badgley  
123 et al., 2017; Camps-Valls et al., 2021). Similar to solar induced chlorophyll fluorescence, they exhibit a linear relationship  
124 with GPP and are considered effective proxies for GPP. Detailed descriptions of all models can be found in Text S1.

125 To reduce uncertainty in GPP estimates from a single model, we used the ERF model, the basic idea of which is to restructure  
126 the simulated values of multiple models. In this study, we directly used the ERF model to establish the relationship between  
127 the GPP simulated by the above six models and GPP observations. In addition, for comparison with the ERF model, we also  
128 used the random forest (RF) method for modeling. In this study, we used average air temperature, minimum air temperature,  
129 VPD, direct solar radiation, diffuse solar radiation, FPAR and LAI to estimate GPP. Both models used the random forest  
130 method, which has been widely used in previous studies of GPP estimate (Jung et al., 2020; Guo et al., 2023). Random forest  
131 is an ensemble learning algorithm that combines the outputs of multiple decision trees to produce a single result, and is  
132 commonly used for classification and regression problems (Belgiu and Drăguț, 2016). In the regression problem, the output  
133 result of each decision tree is a continuous value, and the average of ~~all decision tree outputs~~ ~~the output results of all decision~~  
134 ~~trees~~ is taken as the final result. An overview of all models used can be found in Table 2.

135 **Table 2.** Overview of the models used in this study.

ID	Model	Input data	Output
1	EC-LUE	FPAR, VPD, AT, SRAD, CO <sub>2</sub>	GPP <sub>EC</sub>
2	Revised-EC-LUE	LAI, VPD, AT, DifSR, DirSR, CO <sub>2</sub>	GPP <sub>REC</sub>
3	kNDVI-GPP	Red band and near infrared band ( <u>MCD43</u> )	GPP <sub>kNDVI</sub>
4	NIRv-GPP	Red band and near infrared band ( <u>MCD43</u> )	GPP <sub>NIRv</sub>
5	VPM	Red band, near infrared band, blue band, shortwave infrared band ( <u>MOD09</u> ), AT, SRAD	GPP <sub>VPM</sub>
6	MODIS	FPAR, SRAD, MINT, VPD	GPP <sub>MODIS</sub>
7	Random forest model (RF)	LAI, FPAR, AT, MINT, VPD, DifSR, DirSR	GPP <sub>RF</sub>
8	Ensemble model based on random forest (ERF)	GPP <sub>EC</sub> , GPP <sub>REC</sub> , GPP <sub>kNDVI</sub> , GPP <sub>NIRv</sub> , GPP <sub>MODIS</sub> , GPP <sub>VPM</sub>	GPP <sub>ERF</sub>

136

#### 137 **2.4 Model parameter calibration and validation**

138 FLUXNET only provides GPP observations and meteorological data, lacking direct measurements for LAI, FPAR, and surface  
 139 reflectance, so ~~only~~ remote sensing data is needed, can be used. Considering the variety of remote sensing data sources, such  
 140 as MODIS and AVHRR, it is evident that calibrating the same GPP model with different remote sensing data can yield varied  
 141 parameters. In addition, the number of sites used to calibrate model parameters is also an important influencing factor for  
 142 model parameters. The original parameters of these models were calibrated with only a limited number of sites (e.g., 95 sites  
 143 for Revised EC-LUE and 104 for NIRv) (Wang et al., 2021; Zheng et al., 2020). Therefore, to reduce the impact of the  
 144 uncertainty of model parameters on simulation results, we did not use original parameters and conducted parameter calibration  
 145 for GPP models across different vegetation types. For EC-LUE, Revised EC-LUE, VPM and MODIS, the Markov chain Monte  
 146 Carlo method was used to calibrate model parameters. Traditionally, the mean of the posterior distribution of parameters is  
 147 taken as the optimal value. However, previous studies have indicated that some model parameters are not well constrained  
 148 when calibrating multiple model parameters (Xu et al., 2006; Wang et al., 2017), so we selected the parameter with the smallest  
 149 root-mean-square error (RMSE) as the optimal parameter in each iteration. For each vegetation type, we randomly selected  
 150 70% of the sites for parameter calibration, and repeated the process 200 times. In order to avoid overfitting, we adopted the  
 151 mean of the 200 calibrated parameters as the final model parameters. Similarly, for the two vegetation index models, we  
 152 randomly selected 70% of the sites in each vegetation type for parameter calibration, ~~repeating~~ the process 200 times  
 153 and using the mean of the 200 calibrated parameters as the final model parameters.

154 After obtaining GPP estimates from the six GPP models, we evaluated the simulation performance of the RF model and the  
 155 ERF model respectively. For both models, we evaluated the model performance using 5-fold cross-validation, where the

156 process was repeated 200 times, and the mean of the 200 GPP estimates was considered the final GPP estimate. In addition,  
157 we used a second validation method where 70% of the data was selected for modeling and only the remaining 30% was  
158 validated, a process that was repeated 200 times. We utilized the determination coefficient ( $R^2$ ) and RMSE as metrics to  
159 evaluate the simulation performance of all models. Additionally, we used the ratio of GPP simulations to GPP observations  
160 (Sim/Obs) to measure whether the model overestimates or underestimates.

## 161 **2.5 Global GPP estimation based on ERF model and its uncertainty.**

162 Based on the ERF model, we estimated global GPP for 2001-2022 (ERF\_GPP). It is important to note that in this process, we  
163 used all the site data to build the model. The uncertainties of ERF\_GPP can be attributed to two primary factors: ~~one is~~ the  
164 influence of the number of GPP observations, ~~and the other is~~ and the influence of the number of features (that is, the simulated  
165 GPP). For the first type of uncertainty, we randomly selected 80% of the data to build a model and simulate the multi-year  
166 average of global GPP. The process was repeated 100 times, yielding 100 sets of multi-year averages of ERF\_GPP. Their  
167 standard deviations were considered as the uncertainty of ERF\_GPP caused by the number of GPP observations. For the second  
168 type of uncertainty, we selected different number of features to build a model and simulate the multi-year average of global  
169 GPP. A total of 56 sets of multi-year averages ~~offer~~ ERF\_GPP were obtained. The standard deviation of different combinations  
170 was considered to be the uncertainty of ERF\_GPP caused by the number of features.

## 171 **2.6 Evaluation of the generalization of different GPP datasets**

172 The majority of flux sites in FLUXNET are concentrated in Europe and North America, it is unclear whether the different GPP  
173 estimation methods are suitable for regions with sparse flux sites. Recently, ChinaFlux has published GPP observations from  
174 several sites, offering an opportunity to evaluate the generalization of different GPP datasets. However, the spatial resolution  
175 of most GPP datasets is  $0.05^\circ$ , and a direct comparison with GPP observations at flux sites is challenging. Therefore, we  
176 extracted  $0.05^\circ$  MODIS land use covering the flux sites. If the vegetation type of the flux site matched the MODIS land use,  
177 the site was used for the analysis. Finally, a total of 12 flux sites were selected (Figure S2), and Table S1 shows the information  
178 of these sites. The same procedure was applied to FLUXNET, resulting in the selection of 52 sites (Figure S2). It should be  
179 noted that due to the absence of meteorological data from some sites in Chinaflux, we did not validate all GPP models at the  
180 site scale (500 m).

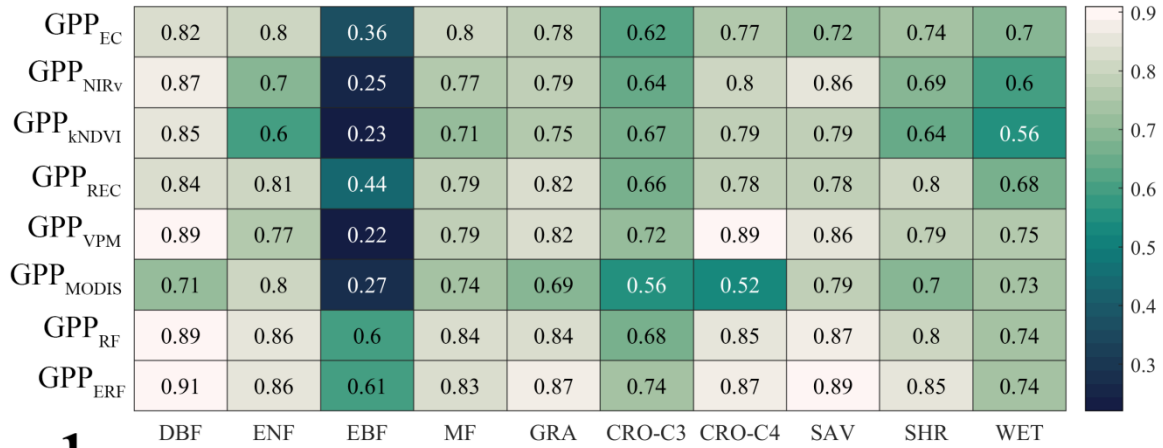
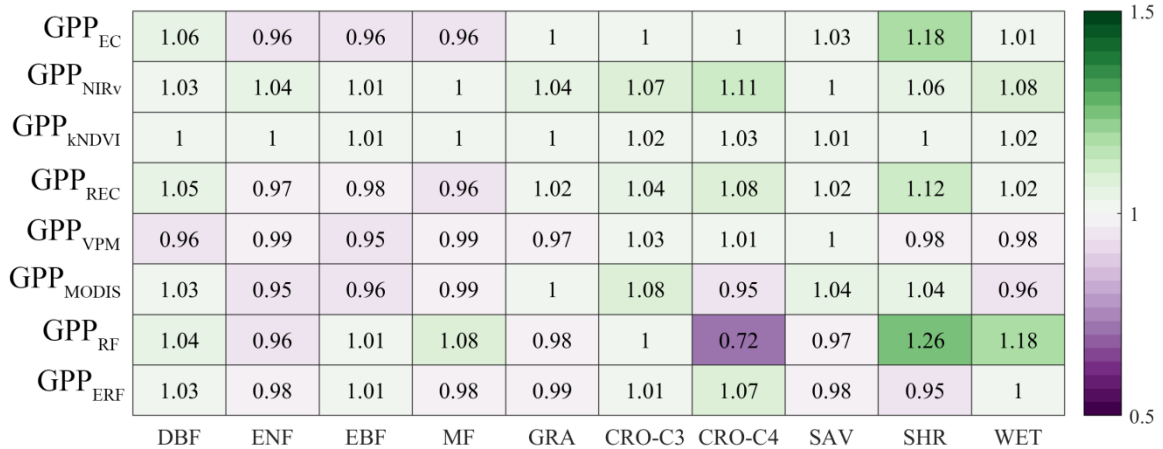
181 We evaluated the generalization of ERF\_GPP at 12 ChinaFlux sites and 52 FLUXNET sites. In addition, we selected a number  
182 of widely used GPP datasets for comparison, including BESS (Li et al., 2023), GOSIF (Li and Xiao, 2019), FLUXCOM: random  
183 forest-based version (FLUXCOM-RF) and ensemble version (FLUXCOM-ENS) (Jung et al., 2020), NIRv (Wang et  
184 al., 2021), Revise-EC-LUE (Zheng et al., 2020), MODIS (Running et al., 2004), VPM (Zhang et al., 2017), which were  
185 generated using different GPP estimation methods. These GPP datasets all have a spatial resolution of 500 m- $0.5^\circ$ , similar to  
186 the resampling process in section 2.1, we have unified them to  $0.05^\circ$ . The common time range for these datasets spanned from  
187 2001 to 2018, and the temporal resolution was unified to monthly to match the GPP observations.

189 **3.1 Performance of GPP models at site scale**

190 Table S2-S7 show the optimization results of the six GPP model parameters. Consistent with ~~the~~ previous study, in the Revised  
191 EC-LUE model, the light use efficiency parameter of shade leaves was significantly higher than that of sunlit leaves (Zheng  
192 et al., 2020). It is necessary to divide ~~the~~ cropland into C3 crops and C4 crops. In all models, the light use efficiency parameters  
193 of C4 crops were significantly higher than those of C3 crops, which was particularly reflected in the two vegetation index  
194 models of  $GPP_{KNDVI}$  and  $GPP_{NIRv}$ , the slope of the linear regression directly reflected the difference in ~~the~~ photosynthetic  
195 capacity of the different crops.

196 Figure 1 shows the performance of all models across different vegetation types. Overall, the performance of the ERF model  
197 was better than that of the other GPP models.  $GPP_{ERF}$  had the higher accuracy among all models, with  $R^2$  between 0.61-0.91  
198 and RMSE between 0.72-2.78  $gC\ m^{-2}\ d^{-1}$ . In contrast, the LUE and vegetation index models performed slightly  
199 weaker, relatively poorly especially in EBF, where  $R^2$  was both below 0.5, in EBF, with  $R^2$  below 0.5. It is worth noting that  
200 compared to other vegetation types, the RMSE was highest for cropland, with 6 out of 8 models for C4 crop exceeding 3  $gC$   
201  $m^{-2}\ d^{-1}$ , suggesting that these existing GPP models may not properly capture the seasonal changes in cropland GPP. The S six  
202 models with calibration parameters and ERF model were found to have no significant deviation across vegetation types.  
203 However,  $GPP_{RF}$  was significantly underestimated for C4 crops and overestimated for SHR.



**a****b****c**

205 **Figure 1.** The performance of the eight models on different vegetation types. a, b and c represent  $R^2$ , RMSE, and Sim/Obs respectively.

206 Combining the results of all flux sites,  $GPP_{ERF}$  explained 85.1% of the monthly GPP variations, while the seven GPP models

207 only explained 67.7%-81.5% of the monthly GPP variations (Figure 2). Another validation method also showed similar results

208 (Figure S3). In order to further prove the robustness of the ERF model, we also used GPP models with original parameters for

209 modeling and validation. As shown in Figure S3S4, the performance of these GPP models decreased significantly, with  $R^2$

210 ranging from 0.570 to 0.719 and RMSE ranging from 2.29 to 3.81  $gC\ m^{-2}\ d^{-1}$ . The phenomenon of "high value underestimation

211 and low value overestimation" was also pronounced. However, the ERF model maintained a consistent advantage, with  $R^2$

212 significantly higher than other GPP models (0.856). In addition, we tested the effect of the amount-number of GPP models on

213 the accuracy of the ERF model. As shown in Table S8, as the number of GPP in the ERF model increased, the performance

214 gain of the model gradually decreased.

215 In summary,  $GPP_{ERF}$  showed high accuracy in terms of vegetation type and the ability to interpret monthly variations in GPP,

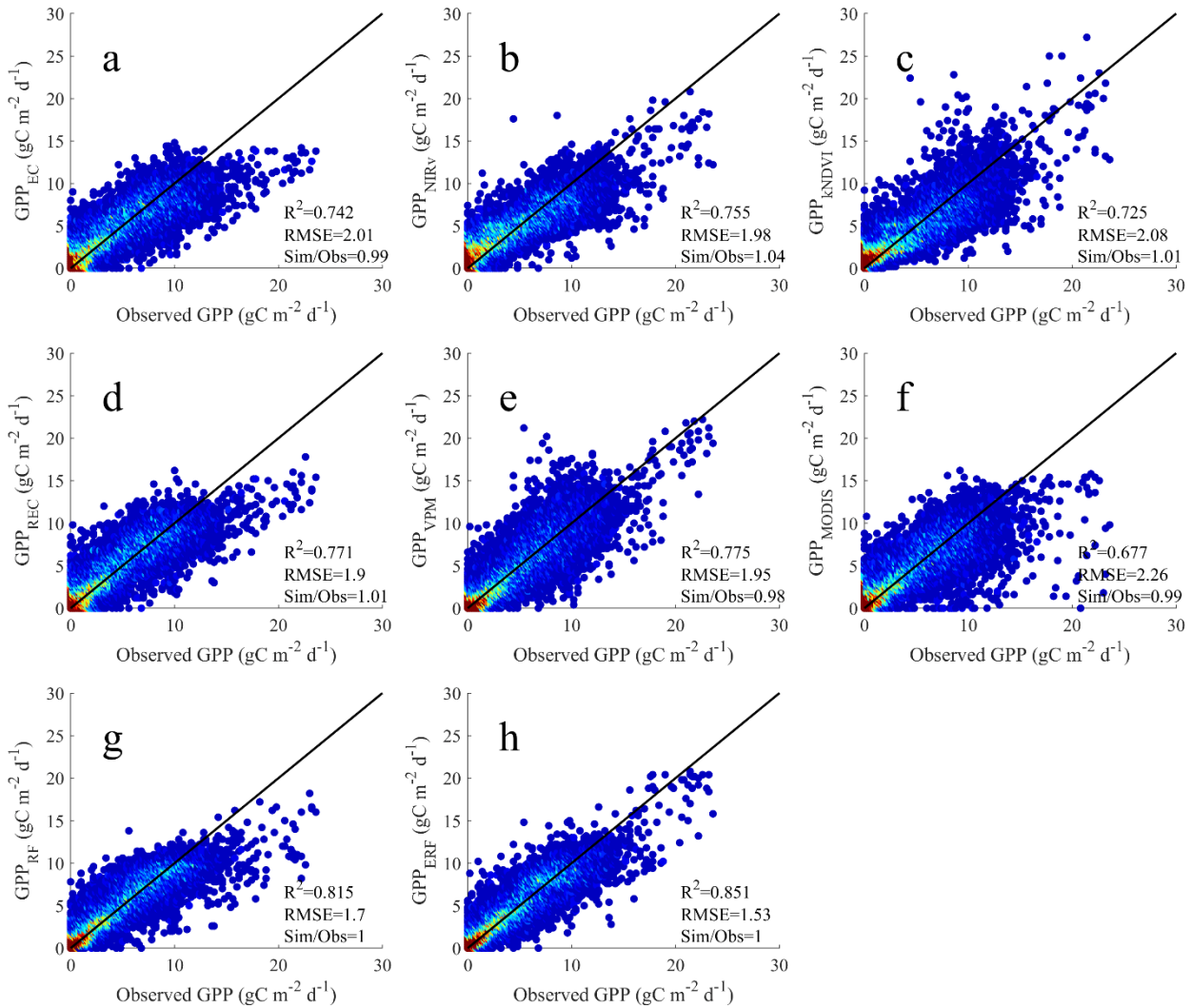
216 which also illustrates the potential of the ERF model to improve GPP estimationone. However, it was observed that most GPP

217 simulations exhibited the phenomenon of "high value underestimation and low value overestimation". For example,  $GPP_{EC}$ ,

218  $GPP_{REC}$ ,  $GPP_{MODIS}$  and  $GPP_{RF}$  showed obvious underestimation in the months when the monthly GPP value surpassed 15  $gC$

219  $m^{-2}\ d^{-1}$  (Figure 2). Therefore, it is necessary to evaluate the performance of different models in each month and different

220 subvalues.



221

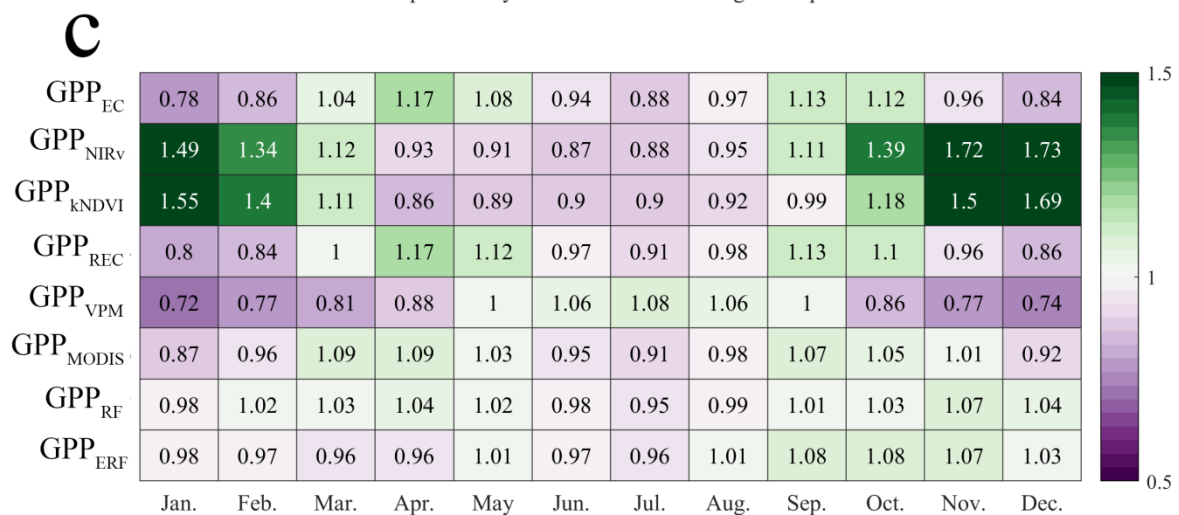
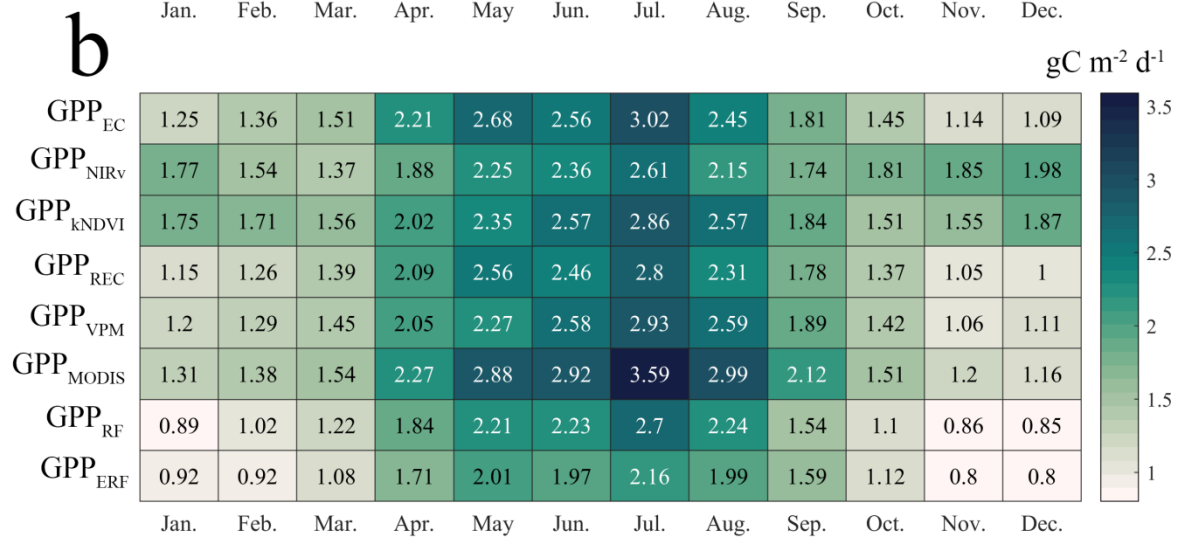
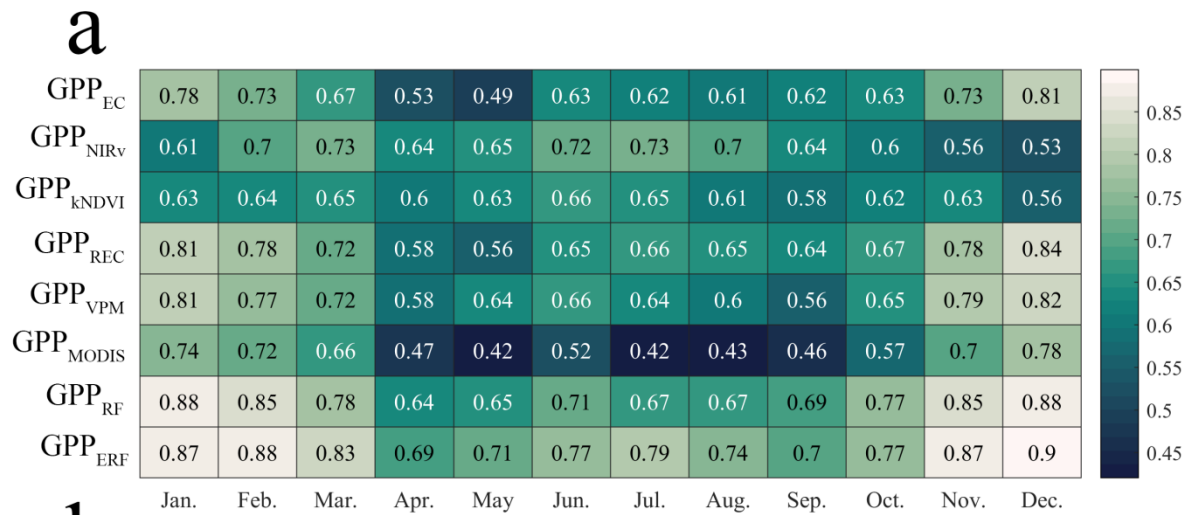
222 **Figure 2.** Comparison between the GPP simulations of the eight models and the GPP observations. a-h represents GPP<sub>EC</sub>, GPP<sub>NIRv</sub>, GPP<sub>KNDVI</sub>,  
 223 GPP<sub>REC</sub>, GPP<sub>VPM</sub>, GPP<sub>MODIS</sub>, GPP<sub>RF</sub>, GPP<sub>ERF</sub>, respectively.

224

### 225 3.2 Performance of GPP models in each month and different subvalues

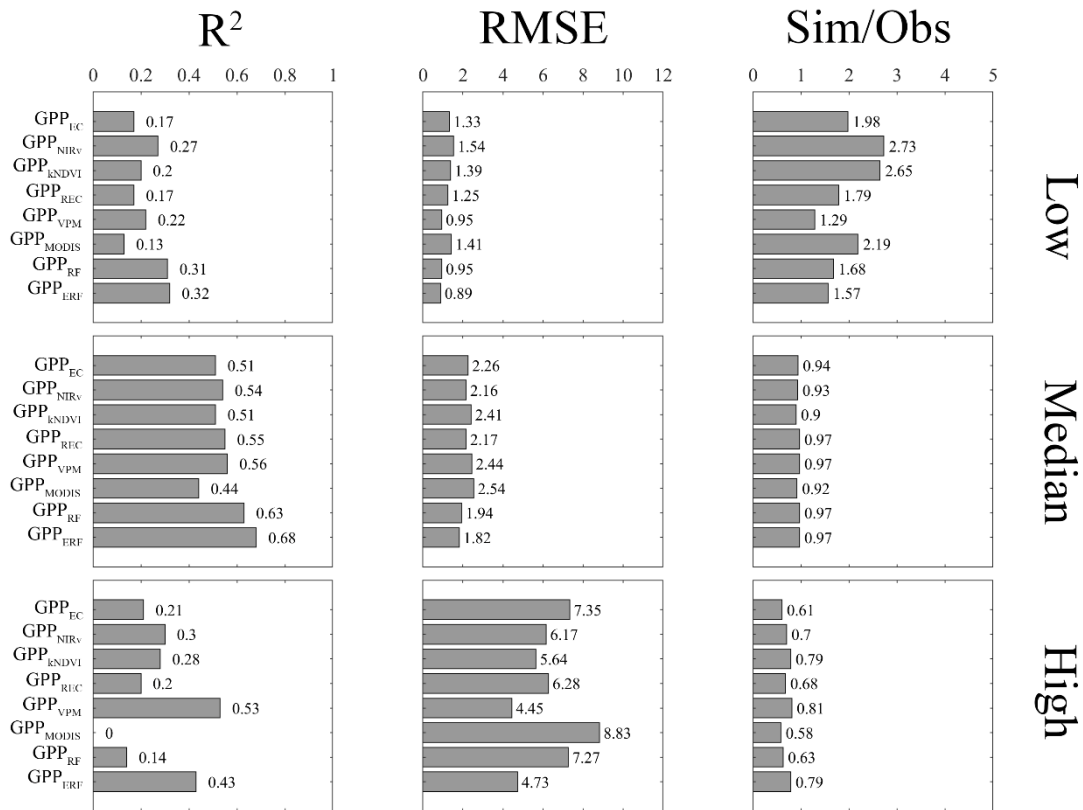
226 Figure 3 shows the simulation accuracy of the eight models in each month. The ERF model maintained a higher accuracy than  
 227 other GPP models, with GPP<sub>ERF</sub> consistently achieving higher  $R^2$  and lower RMSE in most months, and no evident  
 228 phenomenons instances of "high value underestimation and low value overestimation". In contrast, the accuracy of other GPP  
 229 models was less satisfactory accuracy, especially during winter (most flux sites are concentrated in the Northern Hemisphere),

230 the LUE models tended to underestimate GPP, and the Sim/Obs remained at 0.72-1.01, although R<sup>2</sup> ~~values~~ were above 0.7.  
231 Meanwhile, the vegetation index models overestimated GPP, Sim/Obs remained at 1.34-1.73, and R<sup>2</sup> ~~values~~ were relatively  
232 low, mostly around 0.6.



234 **Figure 3.** Performance of the eight models in each month. a, b and c represent  $R^2$ , RMSE, and Sim/Obs respectively.

235 We compared the performance of all models in different subvalues, including high value ( $GPP > 15 \text{ gC m}^{-2} \text{ d}^{-1}$ ), median value  
 236 ( $15 \text{ gC m}^{-2} \text{ d}^{-1} > GPP > 2 \text{ gC m}^{-2} \text{ d}^{-1}$ ), low value ( $GPP < 2 \text{ gC m}^{-2} \text{ d}^{-1}$ ). For extreme values, most models performed poorly  
 237 (Figure 4), with  $R^2$  for GPP models falling below 0.3, and only  $GPP_{VPM}$  showing better performance in the high\_value\_range.  
 238  $GPP_{ERF}$  demonstrated some improvement in both low and high values, with  $R^2$  0.32 and 0.43, RMSE of 0.89 and 4.73  $\text{gC m}^{-2}$   
 239  $\text{d}^{-1}$ , and Sim/Obs closer to 1, respectively. In the median value\_range, all models performed wellbetter, with no significant bias  
 240 in the GPP estimation. The  $R^2$  of GPP models ranged from 0.44 to 0.68, and the RMSE remained between 1.82 and 2.54  $\text{gC}$   
 241  $\text{m}^{-2} \text{ d}^{-1}$ . Further analysis was made at two typical sites, it was obvious that  $GPP_{EC}$ ,  $GPP_{REC}$  and  $GPP_{MODIS}$  on CN-Qia exhibited  
 242 obvious underestimation during the growing season (Figure S4S5). On CH\_Lae,  $GPP_{KNDVI}$  and  $GPP_{VPM}$  were significantly  
 243 overestimated (Figure S5S6). In contrast, at both sites,  $GPP_{ERF}$  was more consistent with observations, indicating that the  
 244 superior performance of  $GPP_{ERF}$  was due to the corrections on the time series.



245

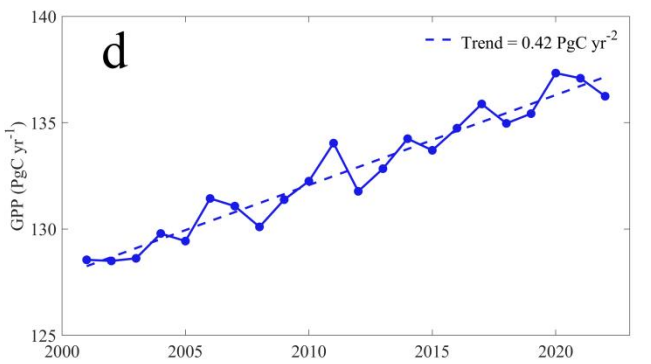
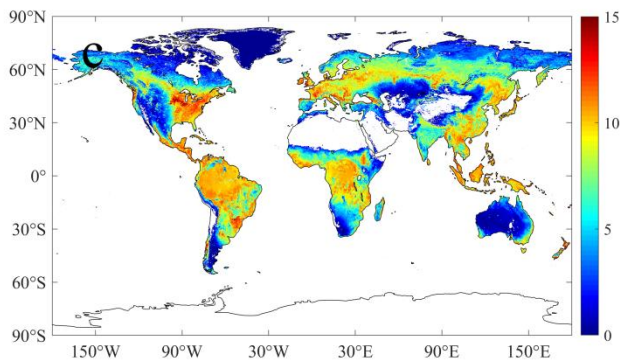
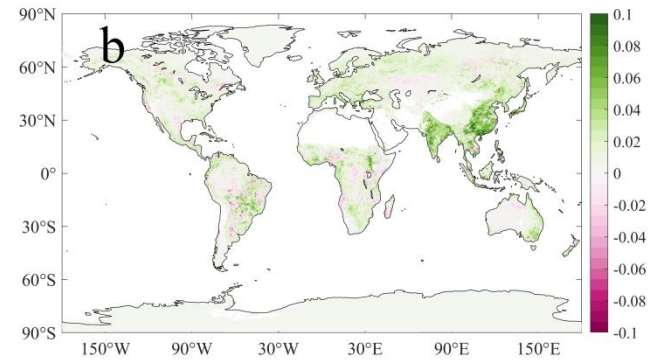
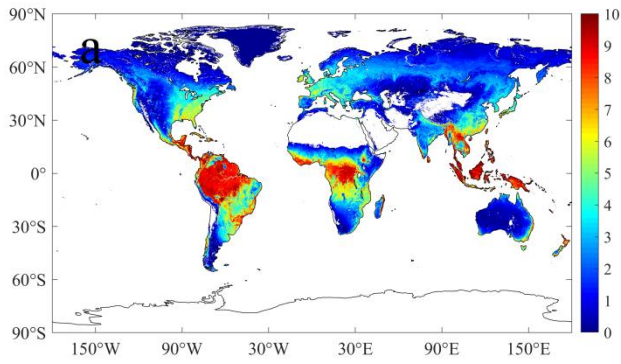
246 **Figure 4.** Performance of eight models in different subvalues.

### 247 3.3 Temporal and spatial characteristics of ERF GPP and its generalization evaluation

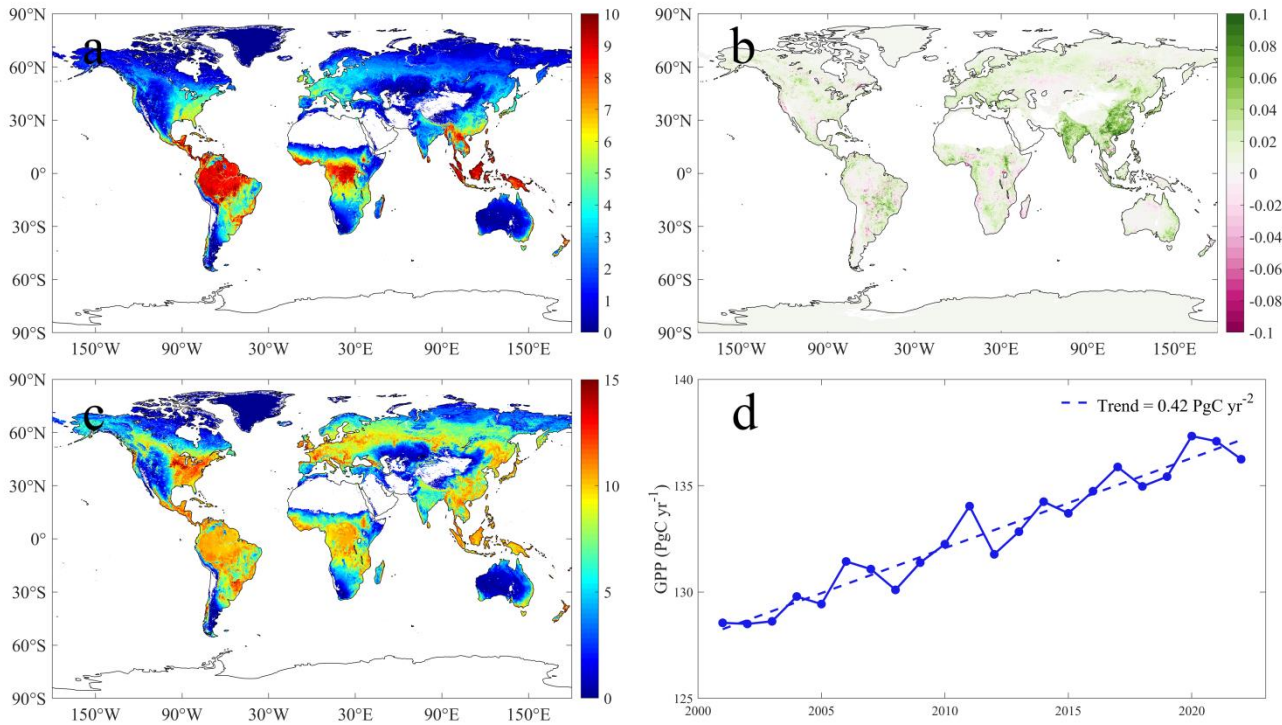
248 Figure 5a shows the spatial distribution of the multi-year average of ERF\_GPP. The high values of GPP ~~waswere~~ mainly  
249 concentrated in tropical areas, exceeding  $10 \text{ gC m}^{-2} \text{ d}^{-1}$ , and relatively high in southeastern North America, Europe and southern  
250 China, about  $4\text{-}6 \text{ gC m}^{-2} \text{ d}^{-1}$ . From 2001-2022, China and India showed the fastest increase in GPP, mostly at  $0.1 \text{ gC m}^{-2} \text{ d}^{-1}$   
251 (Figure 5b), similar to a previous study that reported that China and India led the global greening (Chen et al., 2019). We  
252 further investigated the annual maximum GPP, as shown in Figure 5c, and the North American corn belt was the global leader  
253 in GPP at more than  $15 \text{ gC m}^{-2} \text{ d}^{-1}$ , compared to only  $10 \text{ gC m}^{-2} \text{ d}^{-1}$  in most tropical forests. In 2001-2022, the global GPP was  
254  $132.7 \pm 2.8 \text{ PgC yr}^{-1}$ , with ~~a~~ an increasing trend of  $0.42 \text{ PgC yr}^{-2}$  (Figure 5d). The lowest value was  $128.6 \text{ PgC yr}^{-1}$  in 2001, and  
255 the highest value was  $136.2 \text{ PgC yr}^{-1}$  in 2020 (~~Figure 5d~~).

256 The results of the two uncertainty analyses consistently indicated that ERF\_GPP exhibited ~~a~~ higher uncertainty in tropical  
257 regions (Figures ~~S6-S7~~ and ~~S7-S8~~), and the uncertainty of ERF\_GPP caused by the number of GPP observations was relatively  
258 small, the standard deviation of 100 simulations was about  $0.3 \text{ gC m}^{-2} \text{ d}^{-1}$  in the tropics and lower in other regions, below  $0.1$   
259  $\text{gC m}^{-2} \text{ d}^{-1}$ . In contrast, the uncertainty of ERF\_GPP caused by the number of features was more pronounced ~~much more~~  
260 ~~uncertain~~, especially when fewer features were included in the models ~~the number of features was small~~. It is worth noting that  
261 when the number of features was five, the uncertainty was already substantially less, and the standard deviation was generally  
262 lower than  $0.5 \text{ gC m}^{-2} \text{ d}^{-1}$ .

263







265

266 **Figure 5.** Spatial distribution and interannual changes of ERF\_GPP during 2001-2022. a represents the multi-year average, b represents the  
 267 trend, c represents the annual maximum, and d represents the interannual change of GPP.

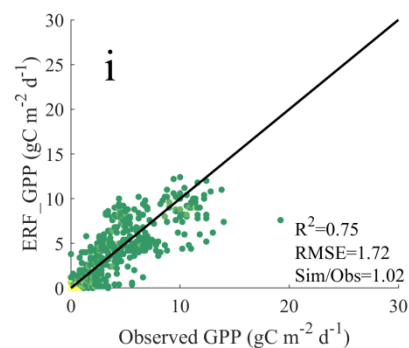
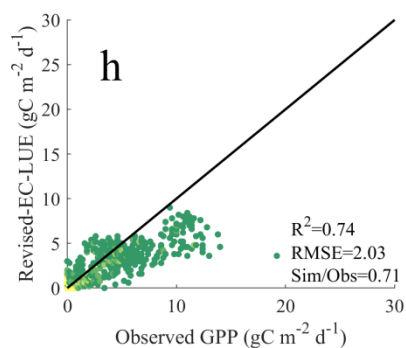
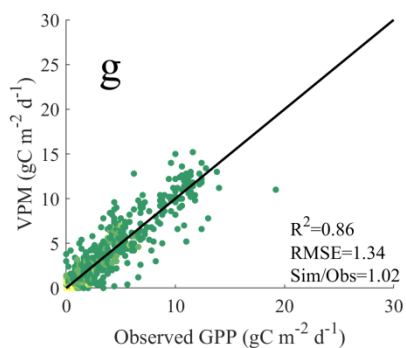
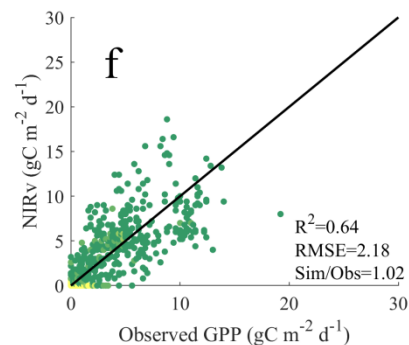
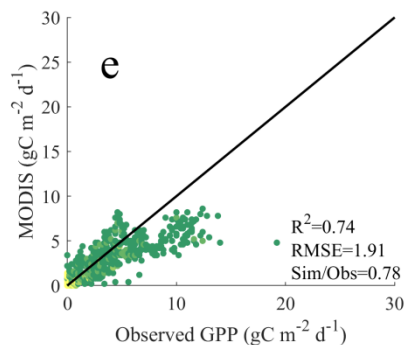
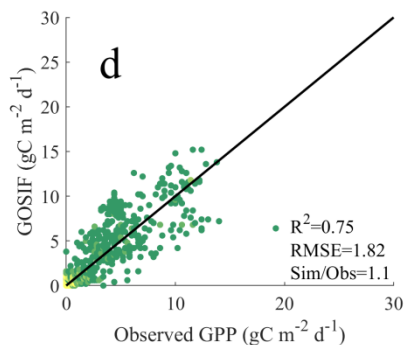
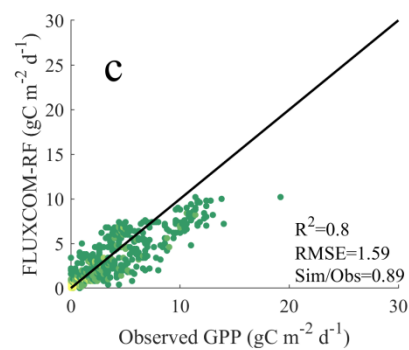
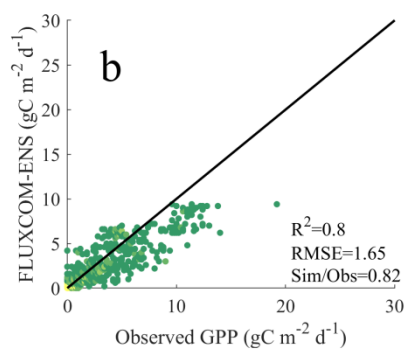
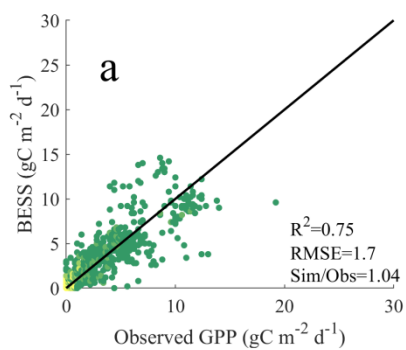
268

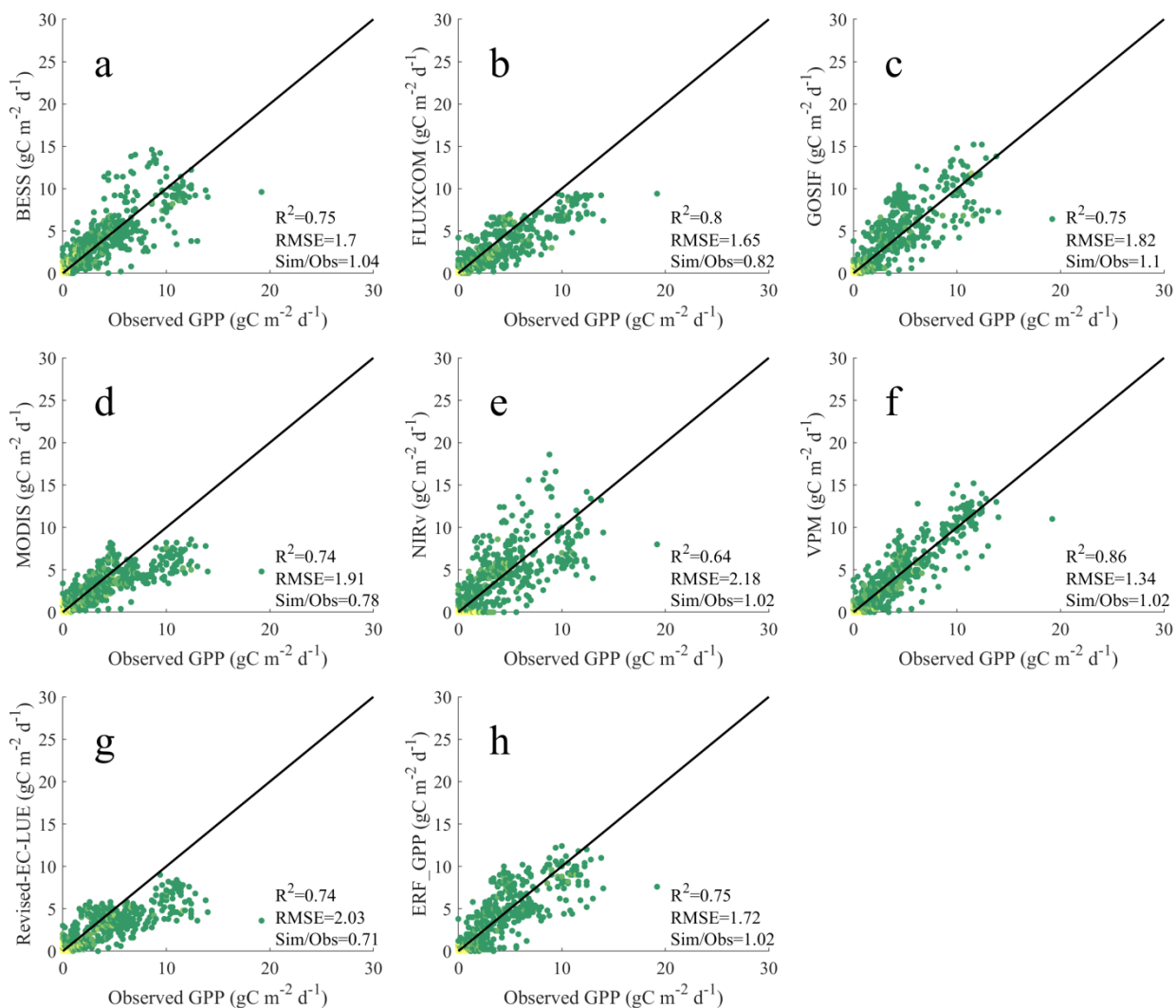
269 As shown in Figure 6, ERF\_GPP and other GPP datasets were validated using GPP observations from ChinaFlux. Among all  
 270 ~~the~~ models, GPP<sub>VPM</sub> demonstrated the best performance, with  $R^2$  of 0.86 and RMSE of  $1.34 \text{ gC m}^{-2} \text{ d}^{-1}$ . ERF\_GPP also  
 271 exhibited high generalization, with  $R^2$  of 0.75, RMSE of  $1.72 \text{ gC m}^{-2} \text{ d}^{-1}$ , there was no “high value underestimation and low  
 272 value overestimation”, which was comparable to the accuracy of BESS and GOSIF. However, the simulation accuracy of the  
 273 other GPP datasets in Chinaflux was relatively poor, with the  $R^2$  of NIRv being only 0.64, while FLUXCOM-ENS,  
 274 FLUXCOM-RE, MODIS and Revised EC-LUE were significantly underestimated, with the Sim/Obs being only 0.71-0.829.  
 275 In the validation of FLUXNET, the  $R^2$  of FLUXCOM-ENS, MODIS, and Revised EC-LUE ranged from 0.57 to 0.67, and the  
 276 RMSE ranged from 2.67 to  $3.3 \text{ gC m}^{-2} \text{ d}^{-1}$ , and exhibited different degrees of underestimation (Figure S8S9). Other GPP  
 277 datasets demonstrated similar performance, with ERF\_GPP being the best ( $R^2 = 0.74$ , RMSE =  $2.26 \text{ gC m}^{-2} \text{ d}^{-1}$ ).

278

279

280





282

283 **Figure 6.** Comparison between the GPP datasets and the GPP observations from ChinaFlux. a-h represents BESS, FLUXCOM-ENS,   
 284 FLUXCOM-RF, GOSIF, MODIS, NIRv, VPM, Revise-EC-LUE, ERF\_GPP, respectively.

## 285 4 Discussion

### 286 4.1 Performance analysis of different models

287 After parameter calibration, both LUE and vegetation index models ~~obtained~~ reliable model accuracy. However,   
 288 noticeable errors persist in different months and subvalues, indicating the prevalent phenomenon of "high value   
 289 underestimation and low value overestimation" (Figures 1-4). In addition to MODIS, the GPP simulated by the other three   
 290 LUE models is generally underestimated in winter (Figure 3), which may be caused by biases in the parameters used in ~~the~~

291 meteorological constraints. In the expression form of the temperature constraint adopted by the LUE models, the maximum  
292 temperature, minimum temperature and optimum temperature for limiting photosynthesis are all constants, however these  
293 values may not be fixed (Huang et al., 2019; Grossiord et al., 2020). A previous study has demonstrated that the GPP  
294 estimation could be effectively improved by using dynamic temperature parameters (Chang et al., 2021). Moreover, the form  
295 of meteorological constraint is also an important influencing factor. Compared with other LUE models, VPM does not use  
296 VPD constraints, but incorporates land surface water index from satellite observations as constraints (Xiao et al., 2004), which  
297 may be the reason why the model performs better than other models at high values (Figure 4). Conversely, the two vegetation  
298 index models overestimated GPP in winter, and even overestimated by 70% in December. The vegetation index model does  
299 not consider meteorological constraints that believe that all environmental impacts on vegetation have been included in the  
300 vegetation index (kNDVI, NIRv). However, it is a fact that under high temperatures or low radiation, the vegetation index may  
301 still maintain the appearance of high photosynthesis (greening), while in fact the GPP is low (Doughty et al., 2021; Yang et  
302 al., 2018; Chen et al., 2024). Furthermore, the relationship between these vegetation indices and GPP is not robust, and the  
303 vegetation indices based on reflectance may have hysteresis (Wang et al., 2022).

304 Compared to other GPP models, the ERF model demonstrated better performance ( $R^2 = 0.851$ ). Since there are no physical  
305 constraints, the machine learning model needs to find the relationship between explanatory variables and target variable from  
306 a large amount of training data (such as  $GPP=f(LAI,T,P, \text{etc.})$ ). Therefore, the reliability of the model usually depends on the  
307 representativeness of the training data. For example, LAI can explain GPP to a large extent, while complex modeling  
308 relationships are still needed from LAI to GPP. The difference between the ERF model and the RF model lies in the explanatory  
309 variables. The ERF model leverages multiple GPP simulations that are more representative and aligned with the target  
310 variable, thus making the GPP simulations more accurate. In other words, the ERF model does not need to take into account  
311 the uncertainties of the model structure (such as meteorological constraints) and model parameters (such as maximum light  
312 use efficiency), but rather focuses on the uncertainties inherent in the simulated GPP. To further clarify the impact of  
313 explanatory variables on the ERF model, we conducted a feature importance analysis (Figure S9S10). From an average of 200  
314 times, the results of the ERF model did not depend on a single GPP simulation. Even  $GPP_{MODIS}$ , with the highest relative  
315 importance, accounted for no more than 25%, suggesting that the ERF model behaves more like a weighted average of multiple  
316 GPP simulations. In addition, it is important to emphasize that the accuracy of the ERF model is still robust even for GPP  
317 simulations of original parameters (Figure S4), which means that we can try to use this method to integrate the currently  
318 published GPP data sets to obtain a more accurate global GPP estimate.

319 It is worth noting that in the study of Tian et al. (2023), the ERF model was also used to improve the GPP estimation. Our  
320 research study extends this work in several ways. Firstly, parameter calibration was carried out in our study so that the final  
321 validation results are comparable, that is, differences in model performance are mainly due to the uncertainty of the model  
322 structure. Secondly, our study focused on the phenomenon of "high value underestimation and low value overestimation" of  
323 GPP model, with results indicating that the ERF model performed well across various vegetation types, months, and subvalues.

324 Finally, we generated the ERF\_GPP dataset and validated it on different observational datasets, further confirming the  
325 robustness of the ERF model in GPP estimation.

## 326 4.2 Robustness of ERF\_GPP

327 ~~In this study, based on site scale validation, we demonstrate the reliability of the ERF model in GPP estimation. However,~~  
328 ~~further discussion is needed regarding the robustness of the spatial distribution, spatial trends and global totals of ERF\_GPP.~~  
329 Since the current GPP datasets are generated based on remote sensing ~~observation~~ and FLUXNET GPP observations, there is  
330 a strong similarity in spatial distribution among all GPP datasets. Therefore, the validation of GPP observations independent  
331 of FLUXNET is crucial. Validation results from GPP observations of ChinaFlux indicated that ~~GPP<sub>ERF</sub>~~ ERF\_GPP exhibited  
332 good generalization in China ( $R^2=0.75$ ), which was slightly lower than the accuracy of 5-fold-cross-validation during modeling,  
333 possibly due to the mismatch between the  $0.05^\circ$  GPP estimate and the footprint of the flux tower (Chu et al., 2021). In addition,  
334 the validation of FLUXNET further confirms the reliability of ERF\_GPP. Overall, this is comparable to or slightly better than  
335 the simulation accuracy of current mainstream GPP datasets. We also observed a clear improvement in the spatial maximum  
336 value of ERF\_GPP in some corn growing regions, such as the North American Corn Belt (Figure 5c), which is supported by  
337 previous studies showing that C4 crops have much higher GPP peaks than other vegetation types (Yuan et al., 2015; Chen et  
338 al., 2011).

339 Due to the ~~increasing trend of drought~~ drought trend, the constraining effect of water on vegetation is gradually increasing, and  
340 some studies have reported the decoupling phenomenon of LAI and GPP under some specific conditions (Jiao et al., 2021; Hu  
341 et al., 2022). However, in China and India ~~that two regions~~ with significant greening, GPP continues to increase in most datasets,  
342 and ERF\_GPP supports this view. This phenomenon may be ~~attributed to~~ due to the low drought pressure on croplands in China  
343 and India due to irrigation, which poses less constraint on GPP (Ambika and Mishra, 2020; Ai et al., 2020). The global estimate  
344 of ERF\_GPP is  $132.7 \pm 2.8$  PgC yr<sup>-1</sup>, which is close to estimates from most previous studies (Wang et al., 2021; Badgley et  
345 al., 2019). A study have suggested that ~~the~~ global GPP may reach 150-175 PgC yr<sup>-1</sup> (Welp et al., 2011), however, there is no  
346 further evidence to support this view.

347 ERF\_GPP exhibited higher uncertainty in tropical regions, similar reports have been made in previously published GPP  
348 datasets (Badgley et al., 2019; Guo et al., 2023). The scarcity of flux observations in these regions (Pastorello et al., 2020),  
349 coupled with the well-known issue of cloud pollution and saturation in remote sensing data in the tropics (Badgley et al., 2019),  
350 exacerbates the uncertainty in GPP estimates for these regions. Therefore, in future studies, on the one hand, more flux  
351 observations in tropical regions are needed, and on the other hand, attempts can be made to combine optical and microwave  
352 data to improve ~~the estimation of~~ GPP estimate.

## 353 4.3 Limitations and uncertainties

354 In this study, we improved GPP estimation based on the ERF model. ~~Nonetheless~~ However, there are still some limitations  
355 and uncertainties due to the availability of data and methods. First, C4 crop distribution maps were used in our study to improve

356 estimates of cropland GPP. However, it is important to note that this dataset only represents the spatial distribution of crops  
357 around the year 2000, which ~~introduce uncertainty into~~~~may add uncertainty to~~ GPP simulations of cropland in a few C3 and  
358 C4 alternating areas. Secondly, the ERF model considers six GPP simulations, and it is not clear whether adding more GPP  
359 simulations to the model can further improve the GPP estimation~~ione~~. Finally, our model did not consider the effect of soil  
360 moisture on GPP, and some previous studies have highlighted the importance of incorporating soil moisture in GPP estimates,  
361 especially for dry years (Stocker et al., 2019; Stocker et al., 2018).

## 362 **5 Conclusion**

363 In this study, we compared the performance of the ERF model with other GPP models at the site scale, especially for the  
364 phenomenon of "high value underestimation and low value overestimation", and further developed the ERF\_GPP dataset.  
365 Overall, GPP<sub>ERF</sub> had higher model accuracy, explaining 85.1% of the monthly GPP variations, and demonstrated reliable  
366 accuracy in different months, vegetation types and subvalues. Over the period from 2001 to 2022, the global estimate of  
367 ERF\_GPP was  $132.7 \pm 2.8$  PgC yr<sup>-1</sup>, corresponding to ~~an increasing~~a trend of 0.42 PgC yr<sup>-2</sup>. Validation results from ChinaFlux  
368 indicated that ERF\_GPP had good generalization. For the current emerging GPP estimation~~ione~~ models, ~~the~~ERF model provides  
369 an alternative ~~GPP-estimation~~-method that lead to better model accuracy.

## 370 **Data and code availability**

371 The ERF\_GPP for 2001-2022 is available at <https://doi.org/10.6084/m9.figshare.24417649> (Chen et al., 2023). The spatial  
372 resolution of ERF\_GPP is 0.05° and the temporal resolution is monthly. Code is available from the author upon reasonable  
373 request.

## 374 **Author contributions**

375 X.C. and T.X.C. conceived the scientific ideas and designed this research framework. X.C. compiled the data, conducted  
376 analysis, prepared figures. X.C., T.X.C. and Y.F.C. wrote the manuscript. D.X.L., R.J.G., J.D., and S.J.Z. gave constructive  
377 suggestions for improving the manuscript.

## 378 **Acknowledgments**

379 This study was supported by the National Natural Science Foundation of China (No. 42130506, 42161144003 and 31570464)  
380 and the Postgraduate Research & Practice Innovation Program of Jiangsu Province (No. KYCX23\_1322).

## 381 Declaration of interests

382 The authors have not disclosed any competing interests.

## 383 References

- 384 Ai, Z., Wang, Q., Yang, Y., Manevski, K., Yi, S., and Zhao, X.: Variation of gross primary production, evapotranspiration and  
385 water use efficiency for global croplands, *Agricultural and Forest Meteorology*, 287, 10.1016/j.agrformet.2020.107935, 2020.
- 386 Ambika, A. K. and Mishra, V.: Substantial decline in atmospheric aridity due to irrigation in India, *Environmental Research*  
387 *Letters*, 15, 10.1088/1748-9326/abc8bc, 2020.
- 388 Anav, A., Friedlingstein, P., Beer, C., Ciais, P., Harper, A., Jones, C., Murray-Tortarolo, G., Papale, D., Parazoo, N. C., Peylin,  
389 P., Piao, S., Sitch, S., Viovy, N., Wiltshire, A., and Zhao, M.: Spatiotemporal patterns of terrestrial gross primary production:  
390 A review, *Reviews of Geophysics*, 53, 785-818, 10.1002/2015rg000483, 2015.
- 391 Badgley, G., Field, C. B., and Berry, J. A.: Canopy near-infrared reflectance and terrestrial photosynthesis, *Science advances*,  
392 3, e1602244, 2017.
- 393 Badgley, G., Anderegg, L. D., Berry, J. A., and Field, C. B.: Terrestrial gross primary production: Using NIRV to scale from  
394 site to globe, *Global change biology*, 25, 3731-3740, 2019.
- 395 Bai, Y., Zhang, S., Bhattarai, N., Mallick, K., Liu, Q., Tang, L., Im, J., Guo, L., and Zhang, J.: On the use of machine learning  
396 based ensemble approaches to improve evapotranspiration estimates from croplands across a wide environmental gradient,  
397 *Agricultural and Forest Meteorology*, 298, 108308, 2021.
- 398 Belgiu, M. and Drăguț, L.: Random forest in remote sensing: A review of applications and future directions, *ISPRS journal of*  
399 *photogrammetry and remote sensing*, 114, 24-31, 2016.
- 400 Camps-Valls, G., Campos-Taberner, M., Moreno-Martínez, Á., Walther, S., Duveiller, G., Cescatti, A., Mahecha, M. D.,  
401 Muñoz-Marí J., García-Haro, F. J., and Guanter, L.: A unified vegetation index for quantifying the terrestrial biosphere,  
402 *Science Advances*, 7, eabc7447, 2021.
- 403 Chang, Q., Xiao, X. M., Doughty, R., Wu, X. C., Jiao, W. Z., and Qin, Y. W.: Assessing variability of optimum air temperature  
404 for photosynthesis across site-years, sites and biomes and their effects on photosynthesis estimation, *Agricultural and Forest*  
405 *Meteorology*, 298, 10.1016/j.agrformet.2020.108277, 2021.
- 406 Chen, C., Park, T., Wang, X., Piao, S., Xu, B., Chaturvedi, R. K., Fuchs, R., Brovkin, V., Ciais, P., Fensholt, R., Tommervik,  
407 H., Bala, G., Zhu, Z., Nemani, R. R., and Myneni, R. B.: China and India lead in greening of the world through land-use  
408 management, *Nature Sustainability*, 2, 122-129, 10.1038/s41893-019-0220-7, 2019.
- 409 Chen, X., Chen, T., Li, X., Chai, Y., Zhou, S., Guo, R., Dai, J.: 2001-2022 global gross primary productivity dataset using an  
410 ensemble model based on random forest. figshare. Dataset. <https://doi.org/10.6084/m9.figshare.24417649.v2>, 2023
- 411 Chen, T., van der Werf, G. R., Dolman, A. J., and Groenendijk, M.: Evaluation of cropland maximum light use efficiency  
412 using eddy flux measurements in North America and Europe, *Geophysical Research Letters*, 38, 10.1029/2011gl047533, 2011.
- 413 Chen, T., Van Der Werf, G., Gobron, N., Moors, E., and Dolman, A.: Global cropland monthly gross primary production in  
414 the year 2000, *Biogeosciences*, 11, 3871-3880, 2014.
- 415 Chen, X., Chen, T., Liu, S., Chai, Y., Guo, R., Dai, J., Wang, S., Zhang, L., and Wei, X.: Vegetation Index-Based Models  
416 Without Meteorological Constraints Underestimate the Impact of Drought on Gross Primary Productivity, *Journal of*  
417 *Geophysical Research: Biogeosciences*, 129, e2023JG007499, 2024.
- 418 Chen, Y., Yuan, H., Yang, Y., and Sun, R.: Sub-daily soil moisture estimate using dynamic Bayesian model averaging, *Journal*  
419 *of Hydrology*, 590, 125445, 2020.
- 420 Chu, H., Luo, X., Ouyang, Z., Chan, W. S., Dengel, S., Biraud, S. C., Torn, M. S., Metzger, S., Kumar, J., and Arain, M. A.:  
421 Representativeness of Eddy-Covariance flux footprints for areas surrounding AmeriFlux sites, *Agricultural and Forest*  
422 *Meteorology*, 301, 108350, 2021.
- 423 Dechant, B., Ryu, Y., Badgley, G., Köhler, P., Rascher, U., Migliavacca, M., Zhang, Y., Tagliabue, G., Guan, K., and Rossini,  
424 M.: NIRVP: A robust structural proxy for sun-induced chlorophyll fluorescence and photosynthesis across scales, *Remote*  
425 *Sensing of Environment*, 268, 112763, 2022.

426 Dechant, B., Ryu, Y., Badgley, G., Zeng, Y., Berry, J. A., Zhang, Y., Goulas, Y., Li, Z., Zhang, Q., and Kang, M.: Canopy  
427 structure explains the relationship between photosynthesis and sun-induced chlorophyll fluorescence in crops, *Remote Sensing*  
428 of Environment, 241, 111733, 2020.

429 Doughty, R., Xiao, X. M., Qin, Y. W., Wu, X. C., Zhang, Y., and Moore, B.: Small anomalies in dry-season greenness and  
430 chlorophyll fluorescence for Amazon moist tropical forests during El Nino and La Nina, *Remote Sensing of Environment*, 253,  
431 10.1016/j.rse.2020.112196, 2021.

432 Grossiord, C., Buckley, T. N., Cernusak, L. A., Novick, K. A., Poulter, B., Siegwolf, R. T., Sperry, J. S., and McDowell, N.  
433 G.: Plant responses to rising vapor pressure deficit, *New Phytologist*, 226, 1550-1566, 2020.

434 Guo, R., Chen, T., Chen, X., Yuan, W., Liu, S., He, B., Li, L., Wang, S., Hu, T., Yan, Q., Wei, X., and Dai, J.: Estimating  
435 Global GPP From the Plant Functional Type Perspective Using a Machine Learning Approach, *Journal of Geophysical*  
436 *Research-Biogeosciences*, 128, 10.1029/2022jg007100, 2023.

437 Hersbach, H., Bell, B., Berrisford, P., Hirahara, S., Horányi, A., Muñoz-Sabater, J., Nicolas, J., Peubey, C., Radu, R., and  
438 Schepers, D.: The ERA5 global reanalysis, *Quarterly Journal of the Royal Meteorological Society*, 146, 1999-2049, 2020.

439 Hu, Z., Piao, S., Knapp, A. K., Wang, X., Peng, S., Yuan, W., Running, S., Mao, J., Shi, X., and Ciais, P.: Decoupling of  
440 greenness and gross primary productivity as aridity decreases, *Remote Sensing of Environment*, 279, 113120, 2022.

441 Huang, M., Piao, S., Ciais, P., Peñuelas, J., Wang, X., Keenan, T. F., Peng, S., Berry, J. A., Wang, K., and Mao, J.: Air  
442 temperature optima of vegetation productivity across global biomes, *Nature ecology & evolution*, 3, 772-779, 2019.

443 Jiao, W., Wang, L., Smith, W. K., Chang, Q., Wang, H., and D'Odorico, P.: Observed increasing water constraint on vegetation  
444 growth over the last three decades, *Nature Communications*, 12, 10.1038/s41467-021-24016-9, 2021.

445 Jung, M., Koirala, S., Weber, U., Ichii, K., Gans, F., Camps-Valls, G., Papale, D., Schwalm, C., Tramontana, G., and Reichstein,  
446 M.: The FLUXCOM ensemble of global land-atmosphere energy fluxes, *Scientific data*, 6, 1-14, 2019.

447 Jung, M., Schwalm, C., Migliavacca, M., Walther, S., Camps-Valls, G., Koirala, S., Anthoni, P., Besnard, S., Bodesheim, P.,  
448 and Carvalhais, N.: Scaling carbon fluxes from eddy covariance sites to globe: synthesis and evaluation of the FLUXCOM  
449 approach, *Biogeosciences*, 17, 1343-1365, 2020.

450 Li, B., Ryu, Y., Jiang, C., Dechant, B., Liu, J., Yan, Y., and Li, X.: BESSv2.0: A satellite-based and coupled-process model  
451 for quantifying long-term global land-atmosphere fluxes, *Remote Sensing of Environment*, 295, 10.1016/j.rse.2023.113696,  
452 2023.

453 Li, X. and Xiao, J.: A Global, 0.05-Degree Product of Solar-Induced Chlorophyll Fluorescence Derived from OCO-2, MODIS,  
454 and Reanalysis Data, *Remote Sensing*, 11, 10.3390/rs11050517, 2019.

455 Monfreda, C., Ramankutty, N., and Foley, J. A.: Farming the planet: 2. Geographic distribution of crop areas, yields,  
456 physiological types, and net primary production in the year 2000, *Global Biogeochemical Cycles*, 22, 10.1029/2007gb002947,  
457 2008.

458 Pastorello, G., Trotta, C., Canfora, E., Chu, H., Christianson, D., Cheah, Y.-W., Poindexter, C., Chen, J., Elbashandy, A., and  
459 Humphrey, M.: The FLUXNET2015 dataset and the ONEFlux processing pipeline for eddy covariance data, *Scientific data*,  
460 7, 1-27, 2020.

461 Pei, Y., Dong, J., Zhang, Y., Yuan, W., Doughty, R., Yang, J., Zhou, D., Zhang, L., and Xiao, X.: Evolution of light use  
462 efficiency models: Improvement, uncertainties, and implications, *Agricultural and Forest Meteorology*, 317, 108905, 2022.

463 Ruehr, S., Keenan, T. F., Williams, C., Zhou, Y., Lu, X., Bastos, A., Canadell, J. G., Prentice, I. C., Sitch, S., and Terrer, C.:  
464 Evidence and attribution of the enhanced land carbon sink, *Nature Reviews Earth & Environment*, 4, 518-534,  
465 10.1038/s43017-023-00456-3, 2023.

466 Running, S. W., Nemani, R. R., Heinsch, F. A., Zhao, M., Reeves, M., and Hashimoto, H.: A continuous satellite-derived  
467 measure of global terrestrial primary production, *Bioscience*, 54, 547-560, 2004.

468 Ryu, Y., Berry, J. A., and Baldocchi, D. D.: What is global photosynthesis? History, uncertainties and opportunities, *Remote*  
469 *sensing of environment*, 223, 95-114, 2019.

470 Stocker, B. D., Zscheischler, J., Keenan, T. F., Prentice, I. C., Penuelas, J., and Seneviratne, S. I.: Quantifying soil moisture  
471 impacts on light use efficiency across biomes, *New Phytologist*, 218, 1430-1449, 10.1111/nph.15123, 2018.

472 Stocker, B. D., Zscheischler, J., Keenan, T. F., Prentice, I. C., Seneviratne, S. I., and Penuelas, J.: Drought impacts on terrestrial  
473 primary production underestimated by satellite monitoring, *Nature Geoscience*, 12, 264-+, 10.1038/s41561-019-0318-6, 2019.



474 Tian, Z., Yi, C., Fu, Y., Kutter, E., Krakauer, N. Y., Fang, W., Zhang, Q., and Luo, H.: Fusion of Multiple Models for  
475 Improving Gross Primary Production Estimation With Eddy Covariance Data Based on Machine Learning, *Journal of*  
476 *Geophysical Research: Biogeosciences*, 128, e2022JG007122, <https://doi.org/10.1029/2022JG007122>, 2023.

477 Wang, J., Dong, J., Yi, Y., Lu, G., Oyler, J., Smith, W., Zhao, M., Liu, J., and Running, S.: Decreasing net primary production  
478 due to drought and slight decreases in solar radiation in China from 2000 to 2012, *Journal of Geophysical Research:*  
479 *Biogeosciences*, 122, 261-278, 2017.

480 Wang, S., Zhang, Y., Ju, W., Qiu, B., and Zhang, Z.: Tracking the seasonal and inter-annual variations of global gross primary  
481 production during last four decades using satellite near-infrared reflectance data, *Science of the Total Environment*, 755,  
482 142569, 2021.

483 Wang, X., Biederman, J. A., Knowles, J. F., Scott, R. L., Turner, A. J., Dannenberg, M. P., Köhler, P., Frankenberg, C., Litvak,  
484 M. E., and Flerchinger, G. N.: Satellite solar-induced chlorophyll fluorescence and near-infrared reflectance capture  
485 complementary aspects of dryland vegetation productivity dynamics, *Remote Sensing of Environment*, 270, 112858, 2022.

486 Welp, L. R., Keeling, R. F., Meijer, H. A. J., Bollenbacher, A. F., Piper, S. C., Yoshimura, K., Francey, R. J., Allison, C. E.,  
487 and Wahlen, M.: Interannual variability in the oxygen isotopes of atmospheric CO<sub>2</sub> driven by El Niño, *Nature*,  
488 477, 579-582, 10.1038/nature10421, 2011.

489 Xiao, J., Chevallier, F., Gomez, C., Guanter, L., Hicke, J. A., Huete, A. R., Ichii, K., Ni, W., Pang, Y., and Rahman, A. F.:  
490 Remote sensing of the terrestrial carbon cycle: A review of advances over 50 years, *Remote Sensing of Environment*, 233,  
491 111383, 2019.

492 Xiao, X., Zhang, Q., Braswell, B., Urbanski, S., Boles, S., Wofsy, S., Moore III, B., and Ojima, D.: Modeling gross primary  
493 production of temperate deciduous broadleaf forest using satellite images and climate data, *Remote sensing of environment*,  
494 91, 256-270, 2004.

495 Xu, T., White, L., Hui, D., and Luo, Y.: Probabilistic inversion of a terrestrial ecosystem model: Analysis of uncertainty in  
496 parameter estimation and model prediction, *Global Biogeochemical Cycles*, 20, 2006.

497 Yang, J., Tian, H. Q., Pan, S. F., Chen, G. S., Zhang, B. W., and Dangal, S.: Amazon drought and forest response: Largely  
498 reduced forest photosynthesis but slightly increased canopy greenness during the extreme drought of 2015/2016, *Global*  
499 *Change Biology*, 24, 1919-1934, 10.1111/gcb.14056, 2018.

500 Yao, Y., Liang, S., Li, X., Chen, J., Liu, S., Jia, K., Zhang, X., Xiao, Z., Fisher, J. B., and Mu, Q.: Improving global terrestrial  
501 evapotranspiration estimation using support vector machine by integrating three process-based algorithms, *Agricultural and*  
502 *Forest Meteorology*, 242, 55-74, 2017.

503 Yao, Y., Liang, S., Li, X., Hong, Y., Fisher, J. B., Zhang, N., Chen, J., Cheng, J., Zhao, S., and Zhang, X.: Bayesian multimodel  
504 estimation of global terrestrial latent heat flux from eddy covariance, meteorological, and satellite observations, *Journal of*  
505 *Geophysical Research: Atmospheres*, 119, 4521-4545, 2014.

506 Yuan, W., Cai, W., Nguy-Robertson, A. L., Fang, H., Suyker, A. E., Chen, Y., Dong, W., Liu, S., and Zhang, H.: Uncertainty  
507 in simulating gross primary production of cropland ecosystem from satellite-based models, *Agricultural and Forest*  
508 *Meteorology*, 207, 48-57, 10.1016/j.agrformet.2015.03.016, 2015.

509 Yuan, W., Cai, W., Xia, J., Chen, J., Liu, S., Dong, W., Merbold, L., Law, B., Arain, A., and Beringer, J.: Global comparison  
510 of light use efficiency models for simulating terrestrial vegetation gross primary production based on the LaThuile database,  
511 *Agricultural and Forest Meteorology*, 192, 108-120, 2014.

512 Yuan, W., Liu, S., Zhou, G., Zhou, G., Tieszen, L. L., Baldocchi, D., Bernhofer, C., Gholz, H., Goldstein, A. H., and Goulden,  
513 M. L.: Deriving a light use efficiency model from eddy covariance flux data for predicting daily gross primary production  
514 across biomes, *Agricultural and Forest Meteorology*, 143, 189-207, 2007.

515 Yuan, W., Zheng, Y., Piao, S., Ciais, P., Lombardozzi, D., Wang, Y., Ryu, Y., Chen, G., Dong, W., and Hu, Z.: Increased  
516 atmospheric vapor pressure deficit reduces global vegetation growth, *Science advances*, 5, eaax1396, 2019.

517 Zhang, Y., Xiao, X., Wu, X., Zhou, S., Zhang, G., Qin, Y., and Dong, J.: A global moderate resolution dataset of gross primary  
518 production of vegetation for 2000–2016, *Scientific data*, 4, 1-13, 2017.

519 Zheng, Y., Shen, R., Wang, Y., Li, X., Liu, S., Liang, S., Chen, J. M., Ju, W., Zhang, L., and Yuan, W.: Improved estimate of  
520 global gross primary production for reproducing its long-term variation, 1982–2017, *Earth System Science Data*, 12, 2725-  
521 2746, 2020.

522

523